small methods
www.small-methods.com

On the Elusive Crystallography of Lithium-Rich Layered Oxides: Novel Structural Models

Arcangelo Celeste, Mariarosaria Tuccillo, Ashok S. Menon, William Brant, Daniel Brandell, Vittorio Pellegrini, Rosaria Brescia, Laura Silvestri, and Sergio Brutti*

Lithium-rich layered oxides (LRLOs) are one of the most attractive families among future positive electrode materials for the so-called fourth generation of lithium-ion batteries (LIBs). Their electrochemical performance is enabled by the unique ambiguous crystal structure that is still not well understood despite decades of research. In the literature, a clear structural model able to describe their crystallographic features is missing thereby hindering a clear rationalization of the interplay between synthesis, structure, and functional properties. Here, the structure of a specific LRLO, $Li_{1.28}Mn_{0.54}Ni_{0.13}Co_{0.02}Al_{0.03}O_2$, using synchrotron X-ray diffraction (XRD), neutron diffraction (ND), and High-Resolution Transmission Electron Microscopy (HR-TEM), is analyzed. A systematic approach is applied to model diffraction patterns of $Li_{1.28}Mn_{0.54}Ni_{0.13}Co_{0.02}Al_{0.03}O_2$ by using the Rietveld refinement method considering the $R\bar{3}m$ and $C2/m$ unit cells as the prototype structures. Here, the relative ability of a variety of structural models is compared to match the experimental diffraction pattern evaluating the impact of defects and supercells derived from the $R\bar{3}m$ structure. To summarize, two possible models able to reconcile the description of experimental data are proposed here for the structure of $Li_{1.28}Mn_{0.54}Ni_{0.13}Co_{0.02}Al_{0.03}O_2$: namely a monoclinic $C2/m$ defective lattice (prototype Li_2MnO_3) and a monoclinic defective supercell derived from the rhombohedral $R\bar{3}m$ unit cell (prototype $LiCoO_2$).

1. Introduction

Lithium-rich layered oxides are a valid alternative to replace current cathode materials for Lithium-ion batteries, thanks to their advantageous transition metal blend composition (Manganese >> Nickel or Cobalt into the oxide stoichiometry), low manufacturing costs, and leading to excellent performance (i.e., discharge specific capacity in the range 200–250 mAh g^{-1}).[1] The crystal structure of LRLO is an open playground of debate,[2,3] based mainly on two hypotheses: a) a two-phase nano-domain[4,5] and b) a single-phase solid solution[6,7] structures. The "nano-domain" hypothesis suggests the coexistence of two phases in the LRLO primary particles, namely, a trigonal $LiTMO_2$ phase (space group $R\bar{3}m$, TM = transition metals), and a monoclinic Li_2MnO_3 phase (space group $C2/m$): both structures are shown in **Figure 1**a,b.

The $LiTMO_2$ phase belongs to a trigonal lattice with $R\bar{3}m$ (166) space group symmetry, in which the structure can be visualized as alternating planes of LiO_6

A. Celeste, M. Tuccillo, S. Brutti
Dipartimento di Chimica
Sapienza Università di Roma
p. le Aldo Moro 5, Rome 00185, Italy
E-mail: arcangelo.celeste@uniroma1.it
A. Celeste
Dipartimento di Chimica e Chimica Industriale
Università degli Studi di Genova
via Dodecaneso 31, Genoa 16146, Italy
A. Celeste, R. Brescia
Istituto Italiano di Tecnologia
Via Morego 30, Genova 16163, Italy
A. Celeste, M. Tuccillo, L. Silvestri
Dipartimento di Tecnologie Energetiche e Fonti Rinnovabili
ENEA C.R. Casaccia
via Anguillarese 301, Rome 00123, Italy
A. S. Menon, W. Brant, D. Brandell
Department of Chemistry–Ångström Laboratory
Uppsala University
Uppsala SE-751 21, Sweden
A. S. Menon
WMG
University of Warwick
Coventry CV4 7AL, UK
V. Pellegrini
BeDimensional Spa
via Torrentesecca 3d, Genoa 16163, Italy
S. Brutti
ISC-CNR OUS Sapienza
Via dei Tarquini, Rome 00185, Italy
S. Brutti
GISEL—Centro di Riferimento Nazionale per i Sistemi di Accumulo Elettrochimico di Energia INSTM
via G. Giusti, Florence 50121, Italy
The ORCID identification number(s) for the author(s) of this article can be found under https://doi.org/10.1002/smtd.202301466

DOI: 10.1002/smtd.202301466

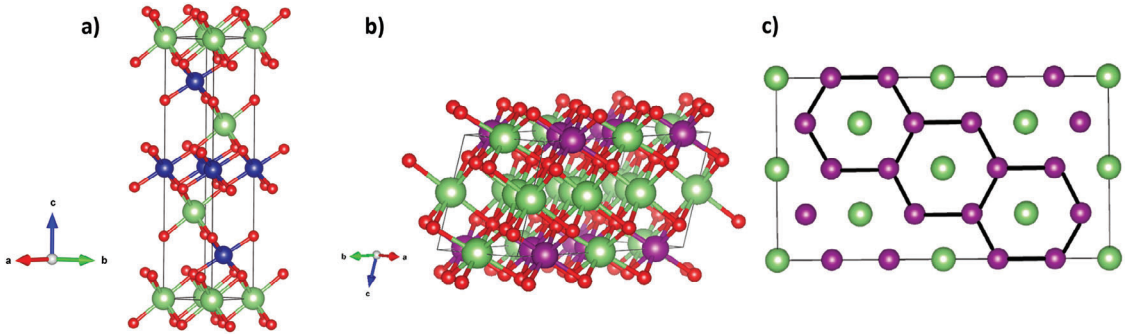

Figure 1. Representation of a) $R\bar{3}m$ and b) $C2/m$ unit cell. c) Hexagonal cation ordering in the TM layer of Li_2MnO_3.

and TMO_6 edge-sharing octahedra.[7,8] A variety of stoichiometric layered oxide materials, such as $LiCoO_2$ and lithium nickel manganese cobalt oxides (NMC), crystallize in this prototypal structure.[9] In the latter, the structure is derived from the $LiCoO_2$ prototype by partially substituting Co with a blend of Mn and Ni, resulting in a TM layer with randomly distributed transition metals.[10–12]

On the other hand, the Li_2MnO_3 structure belongs to the monoclinic crystal class with $C2/m$ (12) space group symmetry.[13–16] It is to be noted that the $C2/m$ unit cell of the Li_2MnO_3 prototype is remarkably similar to that of rhombohedral $LiCoO_2$ with the $R\bar{3}m$ space group: in both cases, the structure is constituted by the stacking of edge-sharing octahedral units. In the case of the rhombohedral structure the stacking along the c axis is given by alternating Li-O-TM-O closed-packed planar layers with an AB-CABC... oxygen layer stacking sequence.

It is to be noted that the Li_2MnO_3 stoichiometry can be reformulated as $Li[Li_{1/3}Mn_{2/3}]O_2$ that better represents the layered crystal structure. In this case, the stacking along the c direction is given by Li-O-(Li, TM)-O closed-packed planar layers with an ABC sequence in the stacking of the oxygen layers. The (Li, TM) layer shows $LiMn_6$ honeycomb motifs, in which each Li is surrounded by six Mn (see Figure 3c).[17,18] This honeycomb ordering results in a twofold axis that breaks the symmetries of the $R\bar{3}m$ space group.[19] As mentioned before, the structure of LRLOs is not fully understood and there is no consensus between the coexistence of two phases or the presence of a single phase.

In particular, according to the nano-domains two-phase model, the general formula of a generic Ni/Co/Mn LRLO material is given by $xLi_2MnO_3{\cdot}(1{-}x)LiNi_aCo_bMn_cO_2$ (where, $0 \leq x \leq 1$ and $a + b + c = 1$)[5] to highlight the coexistence of crystallites with different crystal identity in the same primary particle.

Conversely, according to the solid-solution model the LRLO crystal structure can be represented by a single-phase solid solution with the formula $Li_{1+x}[NiCoMn]_{1-x}O_2$ (where, $1 < x \leq 1/3$). Under this hypothesis, the unit cell belongs to the $C2/m$ space group symmetry but the 3D periodicity of the crystallite is disrupted both in the c-axis stacking and across the ab layers. The resulting large concentrations of stacking faults and Li/TM intra-layer anti-site defects that break the $LiTM_6$ motifs reduce the $C2/m$ unit cell symmetry to an apparent $R\bar{3}m$ lattice in the long range. These large defects result in an ambiguous lattice symmetry and currently, a unique structure for LRLO solid solutions is missing[20–22]: this lack is hindering the facile applicability of this model to the huge variety of LRLO published in the literature.

In the literature, it is possible to find many references to support either structure model. For example, Lu et al. reported a solid solution structure for $Li_{1+x}Ni_{1/3-2x/3}Mn_{2/3-x/3}O_2$ due to the changes in the lattice parameters with the Li content, based on X-ray Diffraction.[23] However, nanodomains of both phases were observed by Kim et al. in an $xLi_2M'O_3{\cdot}(1{-}x\ LiMn_{0.5}Ni_{0.5}O_2$ (M′ = Ti, Mn, Zr; $O \leq x \leq 0.3$) series, using nuclear magnetic resonance spectroscopy.[24] High-resolution TEM images, reported by Shojan et al.,[25] clearly showed well-defined lattice fringes of two different phases and, recently, the nanodomains hypothesis was confirmed by TEM analysis by Wu et al. on a Co-free LRLO.[26] On the other hand, many authors proved the formation of a solid solution of the $C2/m$ and $R\bar{3}m$ lattice symmetries in a variety of LRLOs using high-resolution transmission electron microscopy (HR-TEM) and selected-area electron diffraction SAED.[7,27] Furthermore, a variety of manufacturing parameters, such as synthesis methods, annealing temperature, stoichiometry, and lithium stoichiometry, have a remarkable impact on the final crystal identity of any LRLO material[28–31] revealing that its structural complexity is strongly related to the defect chemistry.[19,30,32]

In this work, our goal is to identify a reliable model to represent the structure of a Co-poor LRLO with stoichiometry $Li_{1.28}Mn_{0.54}Ni_{0.13}Co_{0.02}Al_{0.03}O_2$ in the frame of the solid solution hypothesis. To this aim, we employ synchrotron X-ray diffraction, neutron diffraction, and HR-TEM to analyze the bulk structure of $Li_{1.28}Mn_{0.54}Ni_{0.13}Co_{0.02}Al_{0.03}O_2$ and compare the ability of a variety of different structural models to simulate and model the experimental diffraction patterns.

$Li_{1.28}Mn_{0.54}Ni_{0.13}Co_{0.02}Al_{0.03}O_2$ is a Co-poor cathode material with a very promising electrochemical performance already demonstrated by us in previous publications.[33,34] Due to this outstanding electrochemical behavior and performance in both lithium half-cells and full-cells, we decided to investigate further its crystal structure, using different structural models. Like in many other cases already reported in the literature[35–37] and despite the excellent electrochemical performance, the structure of this phase is only qualitatively understood due to the lack of a reliable structural model. As a consequence, this missing piece of information hinders a rational decoupling and quantification of the impact of the many various effects (e.g., composition, synthesis procedure) that may drive the ability of any LRLO to

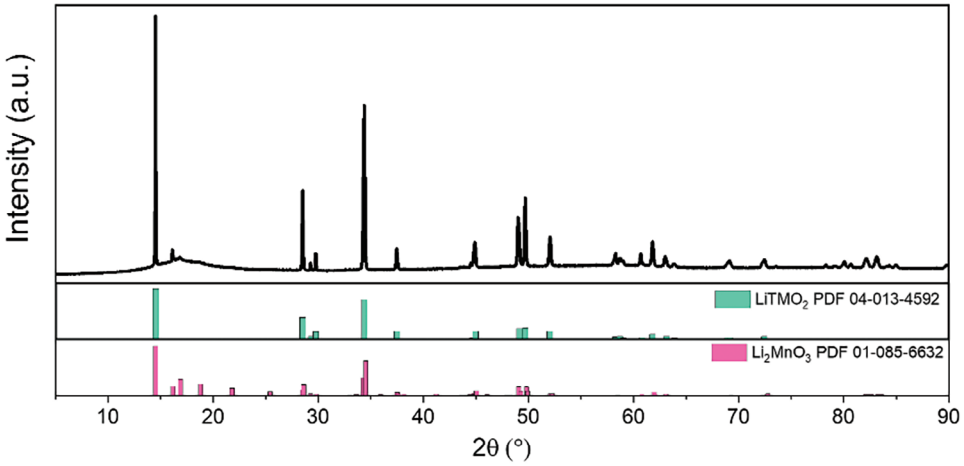

Figure 2. Synchrotron XRD pattern of $Li_{1.28}Mn_{0.54}Ni_{0.13}Co_{0.02}Al_{0.03}O_2$. PDF cards 01-013-4592 ($LiMn_{0.33}Ni_{0.33}Co_{0.33}O_2$) and 01-085-6632 ($Li_2MnO_3$) are used as references.

successfully de-intercalate/intercalate lithium ions reversibly in aprotic batteries.

To shed light on this elusive crystal structure, here, we compare the ability of crystallographic models based on the $R\bar{3}m$ and $C2/m$ unit cells to match the experimental diffraction patterns of $Li_{1.28}Mn_{0.54}Ni_{0.13}Co_{0.02}Al_{0.03}O_2$. In particular, we compare the explicit representation of defects (e.g., anti-sites, vacancies, stacking faults, metals mixing) and the use of supercells derived from the $R\bar{3}m$ structure. Our aim is to identify a realistic model able to: a) match all the relevant diffraction features, b) mimic the selective anisotropic broadening of some diffraction reflections observed in all LRLO, and c) allow the easy evaluation of quantitative descriptors of the crystal structure by the Rietveld refinement of standard X-ray diffraction data. In this work, structural models with increasing structural complexity have been used but are capable of properly matching our datasets going beyond the simple $R\bar{3}m$ and $C2/m$ unit cells that are unable to fit part of the X-ray diffraction pattern or index FFT pattern from HR TEM micrographs.

2. Results and Discussion

2.1. *R*-3*m* and *C*2/*m* Unit Cells Models

The synchrotron X-ray diffraction (XRD) pattern of $Li_{1.28}Mn_{0.54}Ni_{0.13}Co_{0.02}Al_{0.03}O_2$ is shown in **Figure 2** and compared to the reference patterns: PDF 01-085-6632 (Li_2MnO_3) and PDF 04-013-4592 ($LiNi_{1/3}Co_{1/3}Mn_{1/3}O_2$). These reference patterns are the most used ones in literature to identify the LRLO structure. As already mentioned, Li_2MnO_3 and $LiNi_{1/3}Co_{1/3}Mn_{1/3}O_2$ has $C2/m$ and $R\bar{3}m$ space group symmetries, respectively. Apparently, the XRD pattern exhibits features of both phases, particularly in the 15–20° angular range where reflections are unavoidably due to the $C2/m$ structure are observed, while the other reflections could be indexed with $R\bar{3}m$ structure.[38] This ambiguity results in the inability of both the $C2/m$ and $R\bar{3}m$ structure models to allow a complete structural reconstruction by the Rietveld Refinement.[39–41]

The XRD pattern of our sample has been analyzed by the Rietveld Method assuming both $R\bar{3}m$ and $C2/m$ structures and the results are shown in **Figure 3**. Both refinements have been carried out by optimizing lattice parameters, atomic positions, and morphological features (size, microstrain). Since from previously reported measurements[33,34] this material did not show any anisotropy, we used the usual size/strain isotropic model to fit the broadening of the diffraction peaks as a function of the scattering vector. The obtained residual function (R) values were 5% and 5.7% for $R\bar{3}m$ and $C2/m$ structures, respectively, and these values are used here as benchmarks. Overall, the fitting obtained using the $R\bar{3}m$ cell exhibits a slightly better R-value, although it clearly fails to fit all peaks between 15° and 26° (see Figure 3c) due to the lack of symmetry-allowed reflections in this region. Additionally, the $C2/m$ structure fails to fit the 15°–26° reflections due to the unrealistic intensities and asymmetric shapes of these symmetry-allowed reflections (Figure 3d). The refined structural parameters are summarized in **Table 1**. In order to evaluate the possible validity of the two-phase mosaic structural model, we also performed a Rietveld refinement with the two phases ($C2/m$ and $R\bar{3}m$) as shown in Figure S1 (Supporting Information). The value of the R-factor obtained at the end of the Rietveld Refinement is 5.1%, in line with the previous ones. Nevertheless, if you consider the ratio "number of observations/number of parameters to be refined" (Z), the results are 106, 87, and 46 for the rhombohedral, the monoclinic, and the two-phase model, respectively. Lower Values mean more parameters to be refined. So despite the double number of refined parameters in the two-phase model compared to the single one, the R-factor is almost the same suggesting the inadequacy of this model.

Overall, despite the acceptable R-values of Rietveld refinements, an accurate evaluation of the diffraction pattern refinements confirms that all the conventional perfect structures are also inadequate to fully describe the structural features of this LRLO material.

A better understating of the crystal structure within selected fragments can be achieved using HR-TEM. An example of an HR-TEM micrograph, and the corresponding FFT, of the LRLO

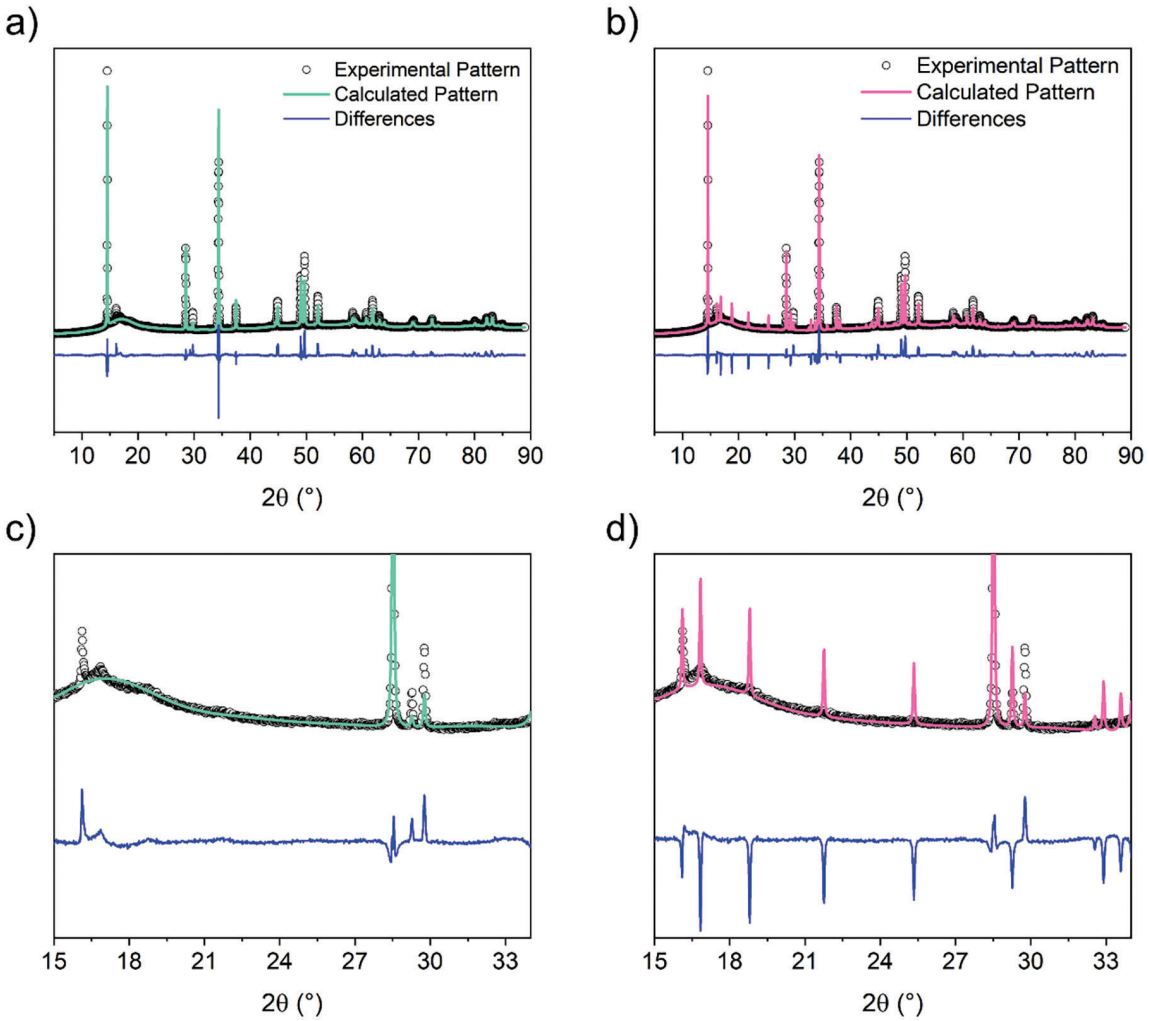

Figure 3. Comparison of Rietveld refinement results using a,c) $R\bar{3}m$ and b,d) $C2/m$ phase.

Table 1. Rietveld refinement results obtained assuming the perfect $C2/m$ and $R\bar{3}m$ structures.

Space group	$C2/m$ ($R = 5.7\%$; $Z = 87$)	$R\text{-}3m$ ($R = 5\%$; $Z = 106$)
Lattice parameters	$a = 4.948$ $b = 8.563$ $c = 5.031$ $\alpha = \gamma = 90°$ $\beta = 109.29°$	$a = b = 2.855$ c = 14.247 $\alpha = \beta = 90°$ $\gamma = 120°$
Atomic position and occupancies (Wyckoff position; OF = occupancy fraction)		
Lithium-ion layer	(2*c*) (0 0 ½) OF(Li) = 1 (4*h*) (0 0.696 ½) OF(Li) = 1	(3*b*) (0 0 ½) OF = 1
Metal ions blend layer	(2*b*) (0 ½ 0) OF(Li) = 0.84 OF(TM) = 0.16 (4*g*) (0 0.167 0) OF(TM) = 1	(3*a*) (0 0 0) OF(Li) = 0.28 OF(TM) = 0.72
Oxygen ions layers	(4*i*) (0.273 0 0.228) OF(O) = 1 (8*j*) (0.239 0.341 0.241) OF(O) = 1	(6*c*) (0 0 0.747) OF = 1

phase is shown in **Figure** 4 where it is not possible to see any clear phase separation.

Indexing of the FFT pattern has been done using the CaRIne Crystallography Software that suggests the identification of possible zone-axes orientations able to match the experimental pattern and estimate the associated errors due to angle and distance mismatch. Apparently, all calculated single-crystal ED patterns derived using the $R\bar{3}m$ unit cells are unable to match any of the FFT patterns collected on the LRLO phase (CaRIne software did not find any compatible zone axis). On the contrary, the $C2/m$ structure is compatible with all FFT patterns, and in particular, the pattern in Figure 4b can be indexed with the [001] zone axis. The representation of the diffraction reflections of the $C2/m$ structure in the reciprocal [001] axis zone is shown in Figure S2a (Supporting Information). Remarkably, a good matching in the FFT pattern indexing using the $R\bar{3}m$ unit cell can be achieved assuming a 3x periodicity along the *a*, *b* lattice parameter directions ($R\bar{3}m_{(3a3bc)}$). The representation of the diffraction spots in the reciprocal [001] axis zone of the $R\bar{3}m_{(3a3bc)}$ cell with (3*a*, 3*b*, *c*) periodicity is shown in Figure S2b (Supporting Information).

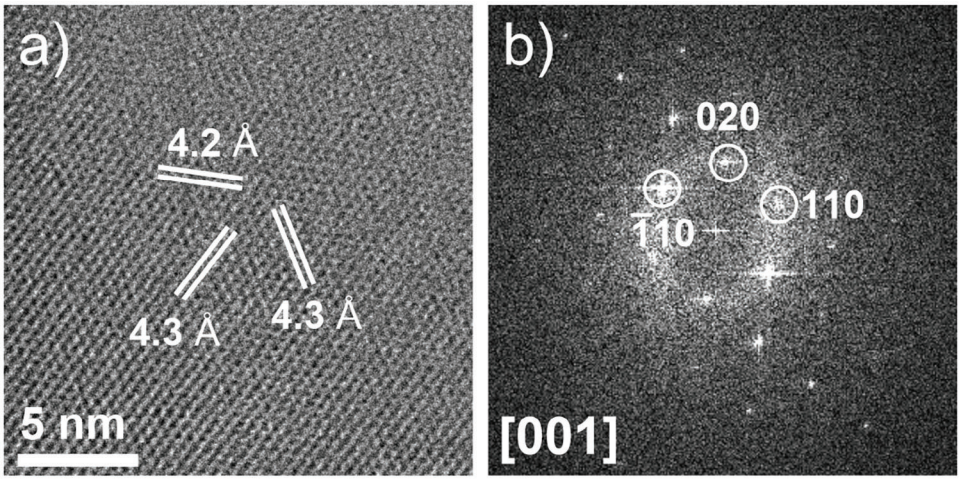

Figure 4. a) HR-TEM image and b) corresponding FFT (indexed using *C*2/*m* unit cell).

Overall, the HR-TEM study also highlights an intricate situation about the structure of LRLO: in the short range, a fingerprint of the *C*2/*m* symmetry is observed, while the $R\bar{3}m$ is fully incompatible unless a rhombohedral supercell is assumed.

In summary, the comparison of crystallographic analyses carried out on HRTEM and synchrotron XRD data assuming the perfect *C*2/*m* and $R\bar{3}m$ lattices highlight very well the complexity of LRLO structure and, the need for an advanced structural model to reconcile XRD and ED results. Based on this experimental evidence, in the next sections, we will compare two different strategies to outline a realistic and reliable advanced model to mimic the structure of LRLO:

- The explicit incorporation of defects in the $R\bar{3}m$ and *C*2/*m* crystal structures
- The occurrence of supercells, i.e., unit cells with one or more lattice directions larger than the primitive cell.

2.2. Defects in $R\bar{3}m$ and *C*2/*m* Structure Models

In order to improve the structure description in $Li_{1.28}Mn_{0.54}Ni_{0.13}Co_{0.02}Al_{0.03}O_2$, anti-site defects between Li and transition metals and oxygen vacancies can be considered in the crystallographic description of both the $R\bar{3}m$ and *C*2/*m* models, using the same synchrotron XRD pattern reported in Figure 2. Anti-site defects are the most ordinary disorder in layered materials and affect the relative peak intensity in the diffraction data. As already reported,[42,43] oxygen vacancies in the anion substructure[44,45] also have the same effect. In **Figure 5**, we show how these two 0D defects can be explicitly modeled in the $R\bar{3}m$ and *C*2/*m* structures by selective modification of the occupancies of specific Wyckoff positions.

Anti-site defects in the $R\bar{3}m$ structure can occur only between the 3*a* site and 3*b* sites (see Figure 5): this kind of defect switches the position of Li and TM ions in two different layers within the unit cell. Actually, we used Ni as a transition metal for the mixing, indeed as reported in the literature, the ionic radii of Li and Ni are very similar.[46] The refinement of the 3*a*/3*b* occupancies converges to an anti-site concentration of 1.5%, leading to a slight improvement in the R-factor (R = 4.98%). Oxygen vacancies in the $R\bar{3}m$ structure can be modeled by refining the occupancy of the 6*c* sites, which has also been reported to occur easily.[34] By simultaneously refining anti-site defects and oxygen vacancies, a final R-factor of 4.9% is obtained for the $R\bar{3}m$ structure with a final chemical formula of $[Li_{0.981}TM_{0.019}]^{3b}[Li_{0.299}TM_{0.701}]^{3a}[O_{1.94}]^{6c}$ (see Table S1, Supporting Information; in the appendix, the corresponding Wyckoff position is reported for each blend/atom).

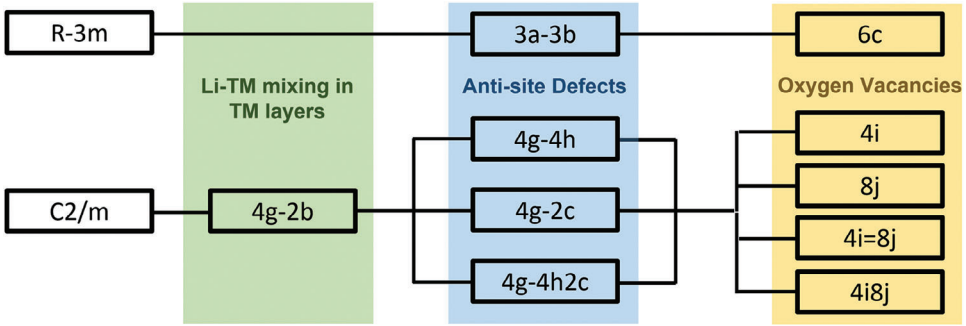

Figure 5. Diagram of different defectivity possibly occurring in the $R\bar{3}m$ and *C*2/*m* models. In the picture, the Wyckoff positions involved are shown. More details are reported in the main text.

These minor reductions in the R-factor are due to a better fitting of the symmetry-allowed diffraction peaks (as in (003) and (104) peaks) whereas the angular region between 15° and 26° is unmodified and, thus, still poorly described (see Figure S3, Supporting Information).

Turning to the monoclinic $C2/m$ model, the description of defects in the occupancies of the metal sites is more complex compared to the $R\bar{3}m$ model, as shown in Figure 5. First, the switch between metals within the TM layers must be considered in the $C2/m$ structure, which cannot be considered in the $R\bar{3}m$ structure (we have only one Wyckoff site in TM layers). In line with the nomenclature used for the $R\bar{3}m$ case, the intra-layer Li/TM switch is indicated as Li-TM mixing whereas the inter-layer Li/TM switch is an anti-site defect. The order in which the parameters were refined is reported in Figure 5, so first Li/TM mixing, then anti-site, and finally oxygen vacancies. Once the parameter is refined, it remains fixed and therefore the following parameters can be refined.

The Li-TM site mixing in the TM layers of the $C/2m$ model occurs between the 4*g* and 2*b* Wyckoff positions and has been refined to a final value of 1.5% mixing. The incorporation of this defect in the $C2/m$ model results in a remarkable improvement in the fitting of (020), (110), (11-1), (021), and (111) reflections (the 15°–26° region of the XRD pattern see Figure S4a,b, Supporting Information) and a drop in the R-factor value from 5.7% to 4%. The final refined crystallographic parameters are reported in Table S2 (Supporting Information).

In the $C2/m$ structure, anti-site defects between different TM and Li layers can be modeled involving different pairs of atomic sites (see Figure 5). We refined the XRD pattern considering three different anti-site switches: i) 4*g*↔4*h*; ii) 4*g*↔2*c*; iii) 4*g*↔4*h*+2*c*. The results of the Rietveld refinements are reported in Figure S4 and Table S3 (Supporting Information). The final R-factors considering both the Li/TM mixing and each of the three different possible configurations of anti-site defect are 3.99%, 3.97%, and 3.98% for cases (i), (ii), and (iii), respectively. All refinements suggest only minor anti-site defectivity between planes (≈1%) with marginal improvement in the fits. Overall, considering that the 4*g*↔2*c* switch was the anti-site defect resulting in the smaller R-factor, it has been included in the following refinement steps.

As a final step, we modeled the occurrence of oxygen vacancies in the $C2/m$ structural model and its impact on the XRD data fitting. Similarly to the anti-site defects, oxygen vacancies can occur from two different Wyckoff sites, namely 4*i* and 8*j*. Four different oxygen vacancy descriptions have been considered by optimizing the atomic occupancies of the different oxygen crystal sites: i) 4i vacancies; ii) 8j vacancies; iii) simultaneous 4i and 8j vacancies with identical concentration; iv) simultaneous 4i and 8j vacancies without constraints. All Rietveld refinements suggest an oxygen occupancy slightly below unity, independent of the vacancy model: the final R-factors marginally decrease to 3.94%, 3.97%, 3.95%, and 3.93% for the (i), (ii), (iii), and (iv) cases, respectively. All Rietveld refinements results are reported in Figure S5 (Supporting Information) as well as the refined parameters (Table S4, Supporting Information).

Overall, the explicit inclusion of 0D defects in both structural models improves the corresponding Rietveld refinement fits. Remarkably, the inclusion of in-plane Li/TM mixing in the $C2/m$ model led to significant improvements in the diffraction data fitting and, generally, all monoclinic models outperform the rhombohedral ones, in line with the experimental evidence by HRTEM.

2.3. Stacking Faults in Monoclinic Unit Cell

According to the previous experimental studies mainly based on selective area diffraction in HRTEM micrographs, many LR-LOs show large concentrations of stacking faults along the *c*-axis.[19,47–50] Qualitative evidence of the impact of the stacking disorder in the simulated XRD pattern of the perfect $C2/m$ structural model is shown in Figure S6 (Supporting Information) for $Li_{1.28}Mn_{0.54}Ni_{0.13}Co_{0.02}Al_{0.03}O_2$ with different degrees of faults (from 0 to 100%, for more details see the experimental details section) by using DIFFaX. Stacking faults affect both diffraction peak intensities and shape, especially in the 15°–26° angular range. In particular, the intensities of the (110), (11$\bar{1}$), (021), and (111) reflections (see Figure S6b, Supporting Information), decrease and broaden remarkably for stacking fault concentrations > 20% and disappear above 40%. Also, the intensity of the (020) reflection at 16.1° decreases while increasing the stacking-fault concentration up to 100% results in a strong asymmetric broadening. On the contrary, the increase in stacking fault concentrations has a negligible impact on the intensity and shape of all the other Bragg peaks. These alterations in the XRD patterns are in line with the experimental data shown in Figure 2 for our LRLO material that shows evidence of a strongly asymmetric peak most indexed by the $C2/m$ (200) reflection.

The structural analysis of the XRD data including stacking faults in the $C2/m$ structure has been carried out using the FAULTS code. Unfortunately, due to software constraints, it is not possible to include in the refinements identical background and peak-shape/broadening functions in GSAS-II to FAULTS and thus, the absolute values of the R-factors are not directly comparable. Therefore, in this section starting again from the perfect $C2/m$ structure, we demonstrate the beneficial impact of the simultaneous incorporation of stacking faults and other 0D defects, and the interplay between these on the diffraction data fit. This hypothesis will be validated by comparing the trend of the R-factors obtained from the FAULTS refinements.

The structural refinement of the un-faulted $C2/m$ structure is shown in Figure S7 (Supporting Information) as well as the optimized lattice parameters and atomic positions (Table S5, Supporting Information). As expected, an unsatisfactory R-value of 8.4% is obtained using the FAULTS code in line with the refinement by GSAS-II. A remarkable improvement in the R-factor and the XRD pattern fitting is obtained by optimizing the stacking fault concentration (see Figure S8 and Table S6, Supporting Information). The refinement suggests a faulting concentration of ≈48% and an R-factor value of 6.7%. From Figure S8a,b (Supporting Information), it is evident how this approach successfully fits the superstructure region similarly to the Li/TM mixing mechanism shown in Section 2.2.

To evaluate the interplay between the stacking fault and the other 0D defects (either Li/TM mixing or anti-sites) we further fit the XRD pattern explicitly considering all defects using FAULTS. The final refinement plot is shown in **Figure 6** and the optimized parameters are summarized in **Table 2**. All defects were refined

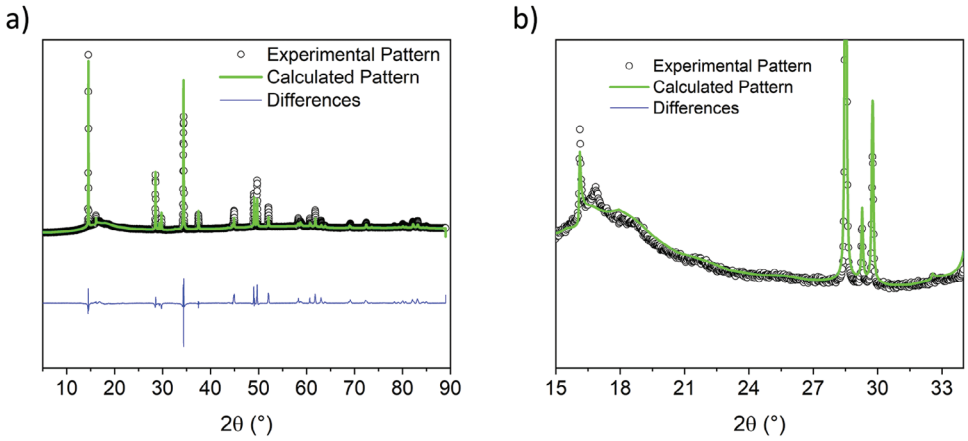

Figure 6. a) FAULTS refinement pattern with all 0D defects and stacking faults. b) Magnified view of the refined data in the 15–35° 2θ range.

Table 2. Values from the FAULTS refinement with stacking faults, Li-TM site mixing, and anti-site defects. The new occupancies are reported in red ($Z = 78$).

Unit cell parameters					
a, b [Å]		**c [Å]**			γ [°]
4.939		4.743			60.06
Layer compositions					
Layer	Atom	x/a	y/b	z/c	Occupancy
L1	Li	0	0	0	1
	Li	1/3	1/3	0	0.916
	Li	2/3	2/3	0	0.916
	TM	1/3	1/3	0	0.084
	TM	2/3	2/3	0	0.084
L2 = L3 = L4	Li	0	0	0	0.622
	TM	0	0	0	0.378
	TM	0.334	0.334	0	0.849
	Li	0.334	0.334	0	0.151
	TM	0.665	0.665	0	0.849
	Li	0.665	0.665	0	0.151
	O	0.358	−0.0158	0.251	1
	O	0.639	0.0117	−0.248	1
	O	−0.0156	0.358	−0.247	1
	O	0.329	0.669	−0.241	1
	O	0.668	0.328	0.243	1
	O	0.011	0.638	0.250	1

step by step, as before, using constraints for the occupancies.

The simultaneous modeling of the 0D defects and the stacking faults leads to a remarkable R-factor decrease of 5.6%. This improvement in the refinement convergence is driven by the simultaneous decrease in the stacking fault concentration from 48 to 40% and an increase of both the Li/TM mixing (in-plane) and li/TM anti-site defects (between planes). This trend suggests a possible overestimation of the stacking disorder if 0D defects are not considered and, vice-versa, an overestimation of the 0D defects if stacking faults are omitted.

Overall, the explicit simultaneous inclusion of stacking faults and 0D defects in the $C2/m$ structural model is mandatory for optimal structural analysis, despite the imperfect match, in terms of improvement of the R-Factor and visual fit of the pattern. As a consequence, the optimal structure model to represent LRLO accounting for all XRD data features is one that simultaneously incorporates in the monoclinic structure prototype the 0D defects (Li/TM mixing, Li/TM anti-site and oxygen vacancies) as well as the stacking fault disorder. It is important to underline the remarkable complexity in the parametrization of stacking faults compared to the use of common Rietveld refinement programs which makes this structural model very challenging.

2.4. Supercell Models

In the previous section, we demonstrated the experimental reconciliation of HRTEM and XRD data by adopting a defective structural model based on a monoclinic structure that incorporates stacking faults and 0D defects (cation anti-site disorder, cation mixing, and oxygen vacancies). Based on the preliminary HRTEM analysis we can also consider a different approach based on the use of supercells derived from the rhombohedral unit cell with 3x periodicity along the *a* and *b* lattice parameters. However, as $R\bar{3}m$ is a non-primitive space group, some preliminary considerations are necessary.

The $C2/m$ space group is a *translationengleiche* subgroup of the $R\bar{3}m$ one, and therefore a primitive unit cell with monoclinic symmetry can be obtained by simple cartesian transformations. Starting from this monoclinic primitive cell, it is possible to create 5 supercells as reported in Table 4 (Experimental Section) that all keep the same symmetry (*klassengleiche* subgroups). In this way, the loss of symmetry constraints allows structural models can be used in the Rietveld refinement analysis of XRD data. These supercell prototypes can distort a perfect "$R\bar{3}m$-like" phase to a more disordered structure. In fact, the use of supercells with larger lattice parameters and multiple atomic sites with similar (but not identical) local coordination allows the simulation of multiple configurations in the atomic distribution in the

Table 3. Refined Lattice parameters and R values obtained with supercells.

Name	Lattice parameter				R [%]	Z
	a	b	c	β		
RC_3a	28.933	2.856	5.023	151.01	4.76	81
RC_3b	9.636	8.563	5.032	151.01	4.11	84
RC_3c	9.644	2.856	15.07	151.01	4.47	73
RC_3a_3b	28.933	8.565	5.023	151.01	4.49	50
RC_3a_b_ac	28.933	2.856	5.787	24.876	5.47	74

transition-metal layer, thus indirectly mimicking the partial ordering along the TM lattice plane.

All the supercell models, as summarized in Table 4, have been tested in the refinement of the synchrotron diffraction pattern of $Li_{1.28}Mn_{0.54}Ni_{0.13}Co_{0.02}Al_{0.03}O_2$ and the results are shown in Figure S9 (Supporting Information). Atomic positions and the other refined parameters are reported in Table S7 (Supporting Information). It is to be noted that, due to the inevitable symmetry reduction induced by the lattice transformations necessary to build the supercells, some diffraction peaks that are systematically extinct in the original $R\bar{3}m$ phase is represented in the diffraction pattern of the 3x supercell models. In fact, as shown in Figure S8 (Supporting Information), supercells show non-null X-ray reflections in the experimental region between 15° and 26°. This allows improvement in the refinement convergence compared to the $R\bar{3}m$ prototype; the Rietveld refinement parameters and convergence ratio are summarized in **Table 3**.

It was expected that a statistical improvement due to the increase in the number of fitted parameters but, actually, R-Factors in Table 3 show how the best values are obtained for the unit cells with reflection in the superstructure region (i.e., RC_3b and RC_3a_3b). Moreover, the comparison of the ratio "number of observations/number of parameters to be refined" between the $R\bar{3}m$ and supercells do not show a huge difference, indeed the ratio are 106, 84, and 50 for $R\bar{3}m$, *RC_3b*, and *RC_3a_3b*, respectively. The improvements in the R-factor are not related only to the increase in the number of refined parameters.

Among the supercells, the *RC_3b* structural model exhibits the best/lowest R-factor value, i.e., 4.11%, a value comparable with that obtained by adopting the *C*2/*m* model with the Li-TM site mixing in the TM layers. In this case, the lattice parameter *b* is three times larger compared to the monoclinic unit cell and this allows to better mimic the distortions in the $LiTM_6$ periodicity along this lattice direction across the TM layers.

To further validate the *RC_3b* supercell model, the impact of several types of defects on the Rietveld refinement convergence quality was checked: overall we adapted the rationale exploited from the *C*2/*m* space group (see Figure 5 for further details). We checked for:

- Anti-site site defects: 4 cases allowed between sites 2*d*-2*a*, 4*g*-4*h*, 2*d*-4*g*, or 4*h*-2*a*. (see Figure S10 and Table S8, Supporting Information, to better visualize the Wyckoff position)
- Li-TM mixing in the transition metals layers: 1 case (4*g* → 2*a*). (see Figure S11 and Table S9, Supporting Information)

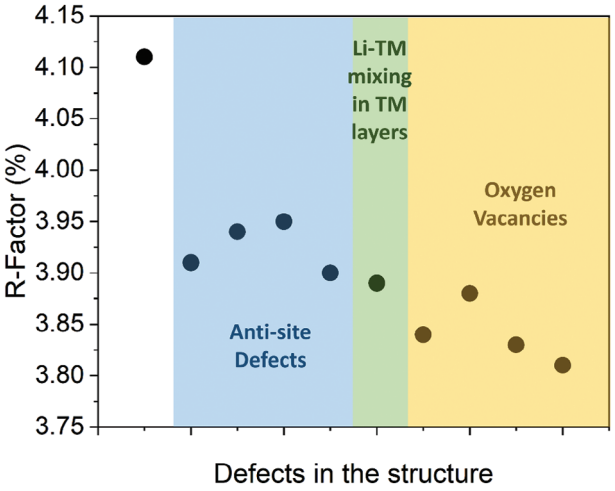

Figure 7. Rietveld refinements results using *RC_3b* with Li-TM mixing, anti-site defects, and oxygen vacancies in 4*i* site.

- Oxygen vacancies: 4 cases: i) oxygen vacancies in 4*i* site; ii) oxygen vacancies in 8*j* site; iii) oxygen vacancies in 4*i* and 8*j* sites with atomic fraction constrained to be equal; iv) oxygen vacancies in 4*i* and 8*j* with atomic fractions unconstrained. (Figure S12 and Table S10, Supporting Information).

All the defective supercell models have been used in the Rietveld Refinement of the XRD pattern of the LRLO material. The impact on the R-factors is shown in **Figure 7**.

All defective supercells lead to better convergences compared to the *RC_3b* model. Looking at the anti-site defects, 4*h*-2*a* and 2*d*-2*a* switches lead to the largest improvements, namely 3.91% and 3.9%, respectively, compared to the R-factor value of the *RC_3b* model. Further improvements have been obtained by considering the Li-TM mixing. In fact, the 4*h*-2*a* metal switch leads to a decrease in the R-factor to 3.89%. As a final point, we also checked the impact of the possible formation of oxygen vacancies. Apparently, oxygen occupancy factors fall below unity in both sites (4*i* and 8*j*) leading to an optimal improvement in the Rietveld refinement convergence, giving the best R-factor value, as low as 3.8%. It is worth noting that additional parameters to refine did not lead to a better R-Factor in all cases.

Overall, the analysis of five supercell models able to mimic both the XRD and HR-TEM data suggests that the optimal prototype able to simulate the LRLO structure reliably is the so-called *RC_3b* model. Furthermore, the best Rietveld refinement of the synchrotron XRD pattern is obtained with the simultaneous inclusion in the R*C_3b* model of (4*h*-2*a*) anti-site defects, (4*g*-2*a*) Li-TM atomic mixing in the TM layer and (4*i* + 8*j*) oxygen vacancies, in line with the case of the monoclinic *C*2/*m* phase (Section 2.2). Remarkably, the Rietveld refinement convergence achieved by the *RC_3b* model (i.e., 3.8%) is slightly better than that obtained with the *C*2/*m* defective lattice (i.e., R = 3.93%) without stacking faults.

2.5. Neutron Diffraction and Electron Diffraction

In the previous sections, two alternate models to mimic the LRLO structure have been discussed and successfully applied to the

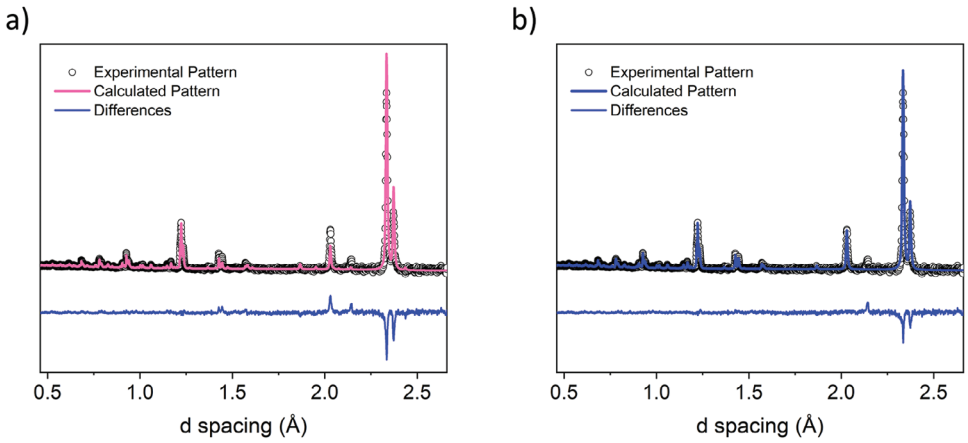

Figure 8. Rietveld refinement analysis of ND data of $Li_{1.28}Mn_{0.54}Ni_{0.13}Co_{0.02}Al_{0.03}O_2$ acquired using detector bank 5 with a) M_{def} and b) SC_{def} unit cell.

Rietveld refinement analysis of synchrotron XRD data. To further validate both these structural models, we applied both prototypes, i.e., *R*C_3*b* and the defective *C*2/*m* lattice without stacking faults to fit the neutron (ND) and the FFTs of HRTEM images of $Li_{1.28}Mn_{0.54}Ni_{0.13}Co_{0.02}Al_{0.03}O_2$ obtained experimentally. ND allows a higher sensitivity to Li and O compared to XRD and, moreover, it is able to distinguish between different transition metals (Mn, Co, Ni) which is impossible with x-ray diffraction.

Specifically, for the refinement of ND and FFT patterns, we adopted the following models:

- Monoclinic unit cell with anti-site defects between 4*g*-2*c*, Li-TM mixing between 4*g*-2*b* crystallographic sites, and oxygen vacancies in 4*i* (M_{def}).
- *R*C_3*b* supercell anti-site defects between 4*h*-2*a*, Li-TM mixing between 4*g*-2*a* sites, and oxygen vacancies in 4*i* (SC_{def}).

The ND pattern is shown in Figure S13 (Supporting Information), the asterisks indicate the Bragg positions due to the vanadium can.[51] The calculated patterns of experimental ND data obtained with the two models are shown in **Figure 8**.

The R-factor values are 3.9% and 3.17%, respectively for the M_{def} and SC_{def} models: the refined lattice parameters are reported in Table S11 (Supporting Information) and, as expected, are in excellent agreement with those refined from the XRD patterns for both lattices. Overall, both structural models can fit the ND pattern, nonetheless, the *R*C_3*b* prototype slightly outperforms the M_{def} defective cell.

Turning to the analysis of FFTs from HR-TEM micrographs, we checked the compatibility of both the M_{def} and SC_{def} models: both models show simulated patterns compatible with the experimental FFT patterns. The calculated ED pattern in the [001] zone axis orientation is shown in Figure S14 (Supporting Information): it apparently converges with a mean error of 11% for both structural models. We also want to point out that the SC_{def} unit cell is different compared to an *R*-3*m* unit cell with 3x periodicity along *a* and *b* used as shown in Section 2.1. On the contrary, this model has considered the periodicity only along the *b*-axis since it is able to fit properly the FFT from HR-TEM and ND.

In summary, the ND and HR-TEM data confirm the reliability of both the structural prototypes selected on the basis of the synchrotron XRD data.

3. Conclusion

The elusive crystal structure of LRLOs has been analyzed for the $Li_{1.28}Mn_{0.54}Ni_{0.13}Co_{0.02}Al_{0.03}O_2$ stoichiometry based on synchrotron X-ray, neutron, and high-resolution TEM datasets. Rietveld refinements have been used to evaluate the relative ability of a variety of structural models to fit the synchrotron XRD patterns. As a starting point, we confirmed the inability of the $R\bar{3}m$ model to explain the HR-TEM and XRD experimental patterns. Moreover, we also proved the inadequacy of nanodomains models, obtaining almost the same results as single-phase models but using a two times larger set of refined parameters. Therefore, we proposed and evaluated the performance, using Rietveld refinement analysis of synchrotron XRD pattern, of a variety of structural prototypes by using GSAS-II in the frame of a single-phase model. We utilized two parallel approaches: a) the simulation of defective *C*2/*m* monoclinic cells and b) the use of supercells derived by simple crystallographic manipulation of the $R\bar{3}m$ unit cell. This analysis allowed us to identify two prototypes, namely M_{def} and SC_{def}, both allowing a satisfactory Rietveld refinement modeling of the XRD patterns. Furthermore, the structural information obtained from the two models is very close. As an example, the mean bond lengths of TM—O pairs in the defective *C*2/*m* and the *R*C_3*b* supercell are 2.011 and 2.028 Å, respectively, indicating a good agreement between the local structure representation obtained from the two models. Both models have been validated on ND and HR-TEM datasets to reconcile all the experimental evidence. Apparently, the SC_{def} prototype, a defective variant of the *R*C_3*b* supercell including anti-site defects, Li-TM mixing, and oxygen vacancies, slightly outperforms the M_{def} model based on a defective *C*2/*m* unit cell including anti-site defects, Li-TM mixing and oxygen vacancies. It is important to recall that further improvements in the XRD fit with the M_{def} model can be obtained by including stacking faults, as proven by the FAULTS analysis. However, stacking faults are very complex to model and handle in standard Rietveld refinement procedures being their automatic optimization unavailable in most codes

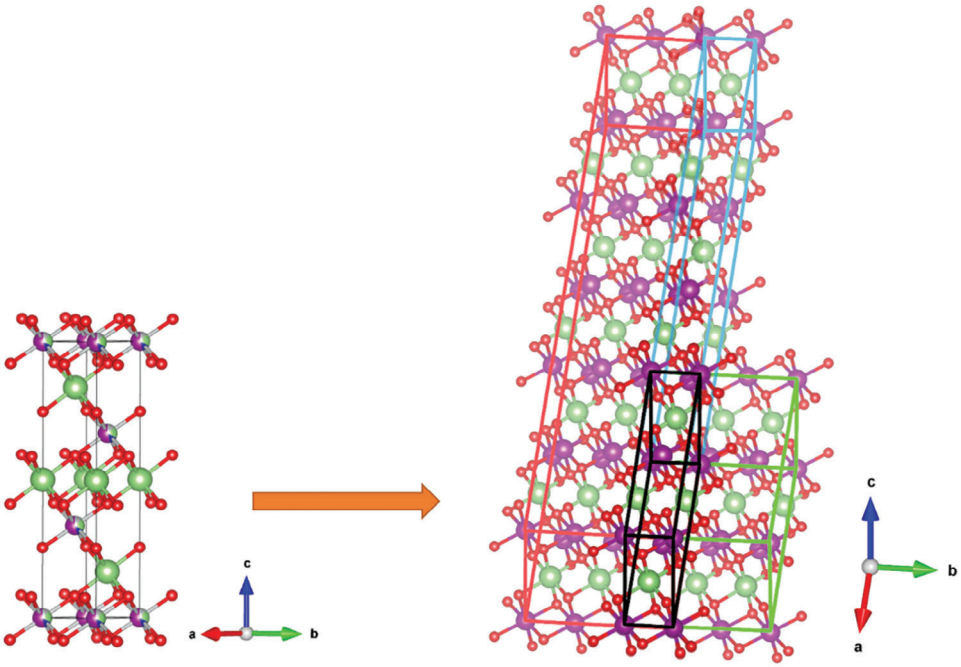

Figure 9. The initial rhombohedral unit cell is reported on the left, with the monoclinic one (black line). Some supercells are reported as examples: the red line represents *RC_3a_3b*, the green line is *RC_3b*, and the blue line represents *RC_3a_b_*ac.

like GSAS-II or MAUD. In summary, either the defective *RC_3b* supercell (SC_{def} prototype), or the defective *C2/m* unit cell (M_{def} prototype), can be adapted to fit the X-ray, neutron, and electron diffraction patterns of the $Li_{1.28}Mn_{0.54}Ni_{0.13}Co_{0.02}Al_{0.03}O_2$ LRLO. As far as we know, this is the first-ever analysis of the elusive structure of LRLO where HR-TEM and XRD experimental evidence are clearly reconciled within the same structural model. Future works should be devoted to understanding the general

Table 4. Summary of unit cells created with PowderCell Software.

Name	Structural model	Lattice parameter				Transformation
		a / Å	*b* / Å	*c* / Å	*β* / °	
R	**Rhombohedral**	**2.8524**	**2.8524**	**14.24**	**90**	
RC	**Monoclinic**	**9.6352**	**2.8524**	**5.0243**	**151.02**	$a = \frac{2}{3}a_R + \frac{1}{3}b_R - \frac{2}{3}c_R$ $b = b_R$ $c = \frac{2}{3}a_R + \frac{1}{3}b_R + \frac{1}{3}c_R$
RC_3a	**Monoclinic**	**28.9055**	**2.8524**	**5.0243**	**151.02**	$a = 3a_{R\_C}$ $b = b_{R\_C}$ $c = c_{R\_C}$
RC_3b	**Monoclinic**	**9.6352**	**8.5572**	**5.0243**	**151.02**	$a = a_{R\_C}$ $b = 3b_{R\_C}$ $c = c_{R\_C}$
RC_3c	**Monoclinic**	**9.6352**	**2.8524**	**15.073**	**151.02**	$a = a_{R\_C}$ $b = b_{R\_C}$ $c = 3c_{R\_C}$
RC_3a_3b	**Monoclinic**	**28.9055**	**8.5572**	**5.0243**	**151.02**	$a = 3a_{R\_C}$ $b = 3b_{R\_C}$ $c = c_{R\_C}$
*RC_3a_b_*ac	**Monoclinic**	**28.9055**	**2.8524**	**5.7775**	**24.916**	$a = 3a_{R\_C}$ $b = b_{R\_C}$ $c = a_{R\_C} + c_{R\_C}$

validity of structural models proposed in this work using LRLOs with different compositions prepared by different synthetic methods. Furthermore, it is mandatory to investigate the correlation between the stacking faults and 0D defects to disclose how this correlation affects the other fitting parameters.

4. Experimental Section

A sol–gel route had been used to synthesize $Li_{1.28}Mn_{0.54}Ni_{0.13}Co_{0.02}Al_{0.03}O_2$, as reported in previous works.[33,34] Stoichiometric amounts of $Mn(CH_3COO)_2{\cdot}4H_2O$ (manganese (II) acetate tetrahydrate, Sigma–Aldrich), $Ni(CH_3COO)_2{\cdot}4H_2O$ (Nickel (II) acetate tetrahydrate, Sigma–Aldrich), $Co(CH_3COO)_2{\cdot}4H_2O$ (cobalt (II) acetate tetrahydrate, Sigma–Aldrich) $(HO)_2Al(CH_3COO)$ (Aluminum acetate dibasic, Sigma–Aldrich), and $LiCH_3COO{\cdot}2H_2O$ (lithium acetate dihydrate, Sigma–Aldrich) were dissolved in ultrapure water. Five percent excess of lithium acetate was used to compensate for the lithium loss during the calcination. An aqueous solution of $C_2H_2O_4$ (oxalic acid, Sigma–Aldrich) ≈0.38 M, acting as a chelating agent, was added to the metal-acetate solution in order to have chelating agent/metals molar ratio of 1.5/1 and left under stirring at 80 °C using an oil bath. The pH was kept at 8 by the addition of ammonia solution (NH_4OH 32%, Sigma–Aldrich). The as-obtained gel was finally completely dried at 200 °C and calcined for 2 h at 450 °C and 12 h at 900 °C.

X-ray diffraction patterns were acquired at the MCX beamline[52] in the ELETTRA synchrotron radiation source, using a wavelength of 1.2 Å (10 keV) in the 2θ range = 5°–90° with a step size of 0.01°. Neutron powder diffraction data were collected on the Polaris time-of-flight powder diffractometer at the ISIS neutron and muon source[53] with samples loaded into cylindrical 6 mm vanadium cans. Refinements of synchrotron X-ray and neutron diffraction patterns were performed with GSAS-II[54] and FAULTS.[55] CIF files of rhombohedral and monoclinic unit cells were downloaded from the PDF-4$^+$ database (PDF 01-085-6632 (Li_2MnO_3) and PDF 04-013-4592 ($LiMO_2$)). The structural models used in the Rietveld refinement had been built with two main approaches: i) supercells and ii) stacking faulted cells.

Supercells were created with PowderCell Software,[56] following the procedure described below. The symmetry of a classical rhombohedral unit cell was downgraded to the primitive monoclinic unit cell. Then, supercells were obtained as larger primitive monoclinic unit cells along one or more lattice directions, without symmetry loss. An overview of all unit cells explored is reported in **Figure 9** and **Table 4** where the last column shows the applied transformation to build the supercells.

The stacking fault simulations of the Li_2TMO_3 monoclinic prototype and the refinement of X-ray data were performed with DIFFaX[57] and FAULTS[55] software. XRD patterns were simulated over 10°–80° (2θ) with a step size of 0.02° and a wavelength of 1.2 Å. For the use of DIFFaX and FAULTS, the conventional monoclinic unit cell was transformed into the triclinic system with P1 space group symmetry. The crystal structure can then be seen in terms of atomic sheets (layers), interconnected via stacking vectors of certain probabilities. Therefore, the degree of (stacking) faulting can be described as the probability of occurrence of stacking/transition vectors. Abraham et al.[58] found that the stacking faults in LRLOs can be properly described with the help of 3 stacking vectors: i) (1/3, −1/3, 1/2); ii) (2/3, 0, 1/2); iii) (0, −2/3, 1/2).

According to the description reported by Serrano et al,[48] two different layers were built: 1) Li layer (L1) and 2) Li-TM-O layer (L2), as reported in **Table 5**. Stacking fault degrees, calculated using the equation reported by Serrano,[48] have been varied, and an infinite number of layers, with a recursive stacking sequence, have been used in the simulation and the refinement. Three different stacking vectors (see Tables 2 and 3) have been used to generate stacking faults in order to have different stacking of the L2 layer with respect to the L1 layer. As can be seen from Table 5, three compositionally identical Li-TM-O layers (L2, L3, and L4) were considered to account for the three different stacking vectors. Therefore, stacking faults are generated by varying the probability of occurrence of each of the stacking vectors and **Table 6** reports the degree of stacking faults and the corresponding probability of occurrence of each of the layers.

Table 5. Details of the structure model used for DIFFaX and FAULTS for $Li_{1.28}Mn_{0.54}Ni_{0.13}Co_{0.02}Al_{0.03}O_2$.

Unit cell parameters					
a, b [Å]		c [Å]			γ [°]
4.9265		4.7416			60.036
Layers composition					
Layer	**Atom**	**x / *a***	**y / *b***	**z / *c***	**Occupancy**
L1	Li	0	0	0	1
	Li	1/3	1/3	0	1
	Li	2/3	2/3	0	1
L2 = L3 = L4	Li	0	0	0	0.84
	TM	0	0	0	0.16
	TM	1/3	1/3	0	1
	TM	2/3	2/3	0	1
	O	0.34	0	0.225	1
	O	0.65	0	–0.225	1
	O	0	0.34	–0.225	1
	O	0.34	0.35	–0.225	1
	O	0.65	0.34	0.225	1
	O	0	0.65	0.225	1
Stacking Vectors					
Transition		**x / *a***	**y / *b***	**z / *c***	
L1→L2		1/3	−1/3	1/2	
L1→L3		2/3	0	1/2	
L1→L4		0	−2/3	1/2	
L2→L1		1/3	−1/3	1/2	
L3→L1		1/3	−1/3	1/2	
L4→L1		1/3	−1/3	1/2	

Table 6. Stacking vectors with their probabilities and the corresponding stacking fault probabilities.

	Translation or Stacking Vectors			Stacking Fault probability [%]
	(1/3, −1/3, ½)	(2/3, 0, 1/2)	(0, −2/3,1/2)	
Translation probabilities	1	0	0	0
	0.9333	0.033	0.033	10
	0.866	0.067	0.067	20
	0.8	0.1	0.1	30
	0.733	0.133	0.133	40
	0.667	0.167	0.167	50
	0.6	0.2	0.2	60
	0.533	0.233	0.233	70
	0.467	0.267	0.267	80
	0.4	0.3	0.3	90
	0.333	0.333	0.333	100

The quality of the agreement between observed and calculated profiles is given by the R-factor, defined as follows:

$$R = 100\frac{\sum_{i=1,n}|y_i - y_{ic}|}{\sum_{i=1,n} y_i} \quad (1)$$

where y_i is the experimental profile intensity and y_{ic} is the number of calculated counts (intensity) at the i-th step. The adoption of the R-factor defined above instead of the commonly used wRp, R_{F2}, and Gof, as a parameter for the accuracy of the fitting procedure, is an inevitable consequence of the use of two different Rietveld refinement programs. Indeed, the R-factor defined above is the only common convergence parameter delivered GSAS-II and FAULTS. Moreover, the ratio "number of observations/number of parameters to be refined", reported as Z, is shown in table refinements.[59]

HRTEM analyses were carried out on a JEOL JEM-2200FS TEM (Schottky emitter), operated at 200 kV, and equipped with a CEOS corrector for the objective lens. HRTEM analysis was carried out by comparing fast Fourier transform (FFT) of single-crystal regions in HRTEM images (small regions of thin fragments) with computed single-crystal diffraction patterns for the structures built in Carine Crystallography software.[]

Supporting Information

Supporting Information is available from the Wiley Online Library or from the author.

Acknowledgements

The XRD synchrotron radiation experiments were performed at the ELETTRA beamline MCX under the frame of the proposal 20195014. The neutron diffraction experiment was carried out at the Polaris beamline of the ISIS Neutron and Muon Source (Oxfordshire, UK), experiment No: 2090129. Thanks are due to Dr Ron Smith for his kind support. The contribution of S.B. and A.C. to this study was carried out within the NEST—Network for Energy Sustainable Transition and received funding from the European Union Next-Generation EU (PIANO NAZIONALE DI RIPRESA E RESILIENZA (PNRR)—MISSIONE 4 COMPONENTE 2, INVESTIMENTO 1.3—D.D. 1561 11/10/2022, B53C22004070006). This manuscript reflects only the authors' views and opinions, neither the European Union nor the European Commission can be considered responsible for them. All Sapienza staff within the NEST project participate in this action under the frame of the grant PE2421852F05911E. A.S.M wishes to acknowledge the support from the Swedish Foundation for Strategic Research (SSF) within the Swedish national graduate school in neutron scattering (SwedNess).

Conflict of Interest

The authors declare no conflict of interest.

Data Availability Statement

The data that support the findings of this study are available from the corresponding author upon reasonable request.

Keywords

crystal structure, Li-rich layered oxide (LRLO), lithium-ion battery, Rietveld refinement, structural models

Received: October 23, 2023
Revised: December 15, 2023
Published online: January 2, 2024

[1] P. Hou, F. Li, H. Zhang, H. Huang, *J. Mater. Chem. A Mater.* **2020**, *8*, 14214.
[2] J. Wang, X. He, E. Paillard, N. Laszczynski, J. Li, S. Passerini, *Adv. Energy Mater.* **2016**, *6*, 1600906.
[3] E. M. Erickson, F. Schipper, T. R. Penki, J.-Y. Shin, C. Erk, F.-F. Chesneau, B. Markovsky, D. Aurbach, *J. Electrochem. Soc.* **2017**, *164*, A6341.
[4] M. M. Thackeray, S.-H. Kang, C. S. Johnson, J. T. Vaughey, S. A. Hackney, *Electrochem. Commun.* **2006**, *8*, 1531.
[5] M. M. Thackeray, C. S. Johnson, J. T. Vaughey, N. Li, S. A. Hackney, *J. Mater. Chem.* **2005**, *15*, 2257.
[6] C. Genevois, H. Koga, L. Croguennec, M. Ménétrier, C. Delmas, F. Weill, *J. Phys. Chem. C* **2015**, *119*, 75.
[7] K. A. Jarvis, Z. Deng, L. F. Allard, A. Manthiram, P. J. Ferreira, *Chem. Mater.* **2011**, *23*, 3614.
[8] M. N. Obrovac, O. Mao, J. R. Dahn, *Solid State Ionics* **1998**, *1*, 9.
[9] L. A. Montoro, M. Abbate, E. C. Almeida, J. M. Rosolen, *Chem. Phys. Lett.* **1999**, *309*, 14.
[10] P. Rozier, J. M. Tarascon, *J. Electrochem. Soc.* **2015**, *162*, A2490.
[11] F. Schipper, E. M. Erickson, C. Erk, J.-Y. Shin, F. F. Chesneau, D. Aurbach, *J. Electrochem. Soc.* **2017**, *164*, A6220.
[12] S. K. Martha, H. Sclar, Z. Szmuk Framowitz, D. Kovacheva, N. Saliyski, Y. Gofer, P. Sharon, E. Golik, B. Markovsky, D. Aurbach, *J. Power Sources* **2009**, *189*, 248.
[13] R. E. Ruther, H. Dixit, A. M. Pezeshki, R. L. Sacci, V. R. Cooper, J. Nanda, G. M. Veith, *J. Phys. Chem. C.* **2015**, *119*, 18022.
[14] V. Massarotti, M. Bini, D. Capsoni, M. Altomare, A. M. G. G. Moliterni, *J. Appl. Crystallogr.* **1997**, *30*, 123.
[15] R. Xiao, H. Li, L. Chen, *Chem. Mater.* **2012**, *24*, 4242.
[16] M. Rossouw, M. Thackeray, *Mater. Res. Bull.* **1991**, *26*, 463.
[17] A. Boulineau, L. Croguennec, C. Delmas, F. Weill, *Chem. Mater.* **2009**, *21*, 4216.
[18] A. D. Robertson, P. G. Bruce, *Chem. Mater.* **2003**, *15*, 1984.

[19] K. A. Jarvis, Z. Deng, L. F. Allard, A. Manthiram, P. J. Ferreira, *J. Mater. Chem.* **2012**, *22*, 11550.
[20] X. Ji, Q. Xia, Y. Xu, H. Feng, P. Wang, Q. Tan, *J. Power Sources* **2021**, *487*, 229362.
[21] S. Zhao, K. Yan, J. Zhang, B. Sun, G. Wang, *Angew. Chem. – Int. Ed.* **2021**, *60*, 2208.
[22] W. Zuo, M. Luo, X. Liu, J. Wu, H. Liu, J. Li, M. Winter, R. Fu, W. Yang, Y. Yang, *Energy Environ. Sci.* **2020**, *13*, 4450.
[23] Z. Lu, D. D. Macneil, J. R. Dahn, *Electrochem. Solid-State Lett.* **2001**, *4*, A191.
[24] J.-S. Kim, C. S. Johnson, J. T. Vaughey, M. M. Thackeray, S. A. Hackney, W. Yoon, C. P. Grey, *Chem. Mater.* **2004**, *16*, 1996.
[25] J. Shojan, V. R. Chitturi, J. Soler, O. Resto, W. C. West, R. S. Katiyar, *J. Power Sources* **2015**, *274*, 440.
[26] C. Wu, S. Cao, X. Xie, C. Guo, H. Li, Z. Li, Z. Zang, B. Chang, G. Chen, X. Guo, T. Wu, X. Wang, *Chem. Eng. J.* **2022**, *429*, 32141.
[27] A. V. Morozov, I. A. Moiseev, A. A. Savina, A. O. Boev, D. A. Aksyonov, L. Zhang, P. A. Morozova, V. A. Nikitina, E. M. Pazhetnov, E. J. Berg, S. S. Fedotov, J.-M. Tarascon, E. V. Antipov, A. M. Abakumov, *Chem. Mater.* **2022**, *34*, 6779.
[28] T. A. Arunkumar, Y. Wu, A. Manthiram, *Chem. Mater.* **2007**, *19*, 3067.
[29] Q. Ma, F. Peng, R. Li, S. Yin, C. Dai, *Mater. Sci. Eng. B Solid State Mater. Adv. Technol.* **2016**, *213*, 123.
[30] T. Matsunaga, H. Komatsu, K. Shimoda, T. Minato, M. Yonemura, T. Kamiyama, S. Kobayashi, T. Kato, T. Hirayama, Y. Ikuhara, H. Arai, Y. Ukyo, Y. Uchimoto, Z. Ogumi, *Chem. Mater.* **2016**, *28*, 4143.
[31] A. S. Menon, S. Ulusoy, D. O. Ojwang, L. Riekehr, C. Didier, V. K. Peterson, G. Salazar-Alvarez, P. Svedlindh, K. Edström, C. P. Gomez, W. R. Brant, *ACS Appl. Energy Mater.* **2021**, *4*, 1924.
[32] Y. Xia, H. Wang, Q. Zhang, H. Nakamura, H. Noguchi, M. Yoshio, *J. Power Sources* **2007**, *166*, 485.
[33] A. Celeste, F. Girardi, L. Gigli, V. Pellegrini, L. Silvestri, S. Brutti, *Electrochim. Acta* **2022**, *428*, 40737.
[34] A. Celeste, R. Brescia, G. Greco, P. Torelli, S. Mauri, L. Silvestri, V. Pellegrini, S. Brutti, *ACS Appl. Energy Mater.* **2022**, *5*, 1905.
[35] E. Zhao, Q. Li, F. Meng, J. Liu, J. Wang, L. He, Z. Jiang, Q. Zhang, X. Yu, L. Gu, W. Yang, H. Li, F. Wang, X. Huang, *Angew. Chem.* **2019**, *131*, 4367.
[36] S.-L. Cui, Xu Zhang, X.-W. Wu, S. Liu, Z. Zhou, G.-R. Li, X.-P. Gao, *ACS Appl. Mater. Interfaces* **2020**, *12*, 47655.
[37] Z. Tai, W. Zhu, M. Shi, Y. Xin, S. Guo, Y. Wu, Y. Chen, Y. Liu, *J. Colloid Interface Sci.* **2020**, *576*, 468.
[38] A. Boulineau, L. Croguennec, C. Delmas, F. Weill, *Solid State Ion.* **2010**, *180*, 1652.
[39] H. Sclar, S. Maiti, R. Sharma, E. M. Erickson, J. Grinblat, R. Raman, M. Talianker, M. Noked, A. Kondrakov, B. Markovsky, D. Aurbach, *Inorganics* **2022**, *10*, 39.
[40] H. Choi, A. R. Schuer, H. Moon, M. Kuenzel, S. Passerini, *Electrochim. Acta* **2022**, *430*, 41047.
[41] H. Liu, Y. Chen, S. Hy, K. An, S. Venkatachalam, D. Qian, M. Zhang, Y. S. Meng, *Adv. Energy Mater.* **2016**, *6*.
[42] H. Dixit, Wu Zhou, J.-C. Idrobo, J. Nanda, V. R. Cooper, *ACS Nano* **2014**, *8*, 12710.
[43] W. Wei, L. Chen, A. Pan, D. G. Ivey, *Nano Energy* **2016**, *30*, 580.
[44] M. Farahmandjou, W.-H. Lai, J. Safaei, S. Wang, Z. Huang, F. Marlton, J. Ruan, B. Sun, H. Gao, K. (.K.). Ostrikov, P. H. L. Notten, G. Wang, *Batter. Supercaps.* **2023**, *6*, e202300123.
[45] Q. Ma, Z. Chen, S. Zhong, J. Meng, F. Lai, Z. Li, C. Cheng, L. Zhang, T. Liu, *Nano Energy* **2021**, *81*, 05622.
[46] L. Yu, H. Zhao, J. Sun, Q. Han, J. Zhu, J. Lu, *Adv. Funct. Mater.* **2022**, *32*, 2204931.
[47] J. Serrano-Sevillano, M. Casas-Cabanas, A. Saracibar, *J. Phys. Chem. Lett.* **2021**, *12*, 7474.
[48] J. Serrano-Sevillano, M. Reynaud, A. Saracibar, T. Altantzis, S. Bals, G. Van Tendeloo, M. Casas-Cabanas, *Phys. Chem. Chem. Phys.* **2018**, *20*, 23112.
[49] R. Shunmugasundaram, R. S. Arumugam, J. R. Dahn, *J. Electrochem. Soc.* **2016**, *163*, A1394.
[50] A. S. Menon, S. Khalil, D. O. Ojwang, K. Edström, C. P. Gomez, W. R. Brant, *Dalton Trans.* **2022**, *51*, 4435.
[51] K. Luo, M. R. Roberts, R. Hao, N. Guerrini, D. M. Pickup, Yi-S Liu, K. Edström, J. Guo, A. V. Chadwick, L. C. Duda, P. G. Bruce, *Nat. Chem.* **2016**, *8*, 684.
[52] L. Rebuffi, J. R. Plaisier, M. Abdellatief, A. Lausi, P. Scardi, *J. Inorg. Gen. Chem.* **2014**, *640*, 3100.
[53] R. I. Smith, S. Hull, M. G. Tucker, H. Y. Playford, D. J. Mcphail, S. P. Waller, S. T. Norberg, *Rev. Sci. Instrum.* **2019**, *90*.
[54] B. H. Toby, R. B. Von Dreele, *J. Appl. Crystallogr.* **2013**, *46*, 544.
[55] M. Casas-Cabanas, M. Reynaud, J. Rikarte, P. Horbach, J. Rodríguez-Carvajal, *J. Appl. Crystallogr.* **2016**, *49*, 2259.
[56] W. Kraus, G. Nolze, *J. Appl. Cryst.* **1996**, *29*, 301.
[57] P. Faults, M. M. J. Treacy, J. M. Newsam, M. W. Deem, M. M. J. Treacyt, J. M. Newsamt, *Proc. Royal Society of London. Series A: Mathematical Phys. Sci.* **1991**, *433*, 499.
[58] J. Bareño, C. H. Lei, J. G. Wen, S.-H. Kang, I. Petrov, D. P. Abraham, *Adv. Mater.* **2010**, *22*, 1122.
[59] A. Altomare, F. Capitelli, N. Corriero, C. Cuocci, A. Falcicchio, A. Moliterni, R. Rizzi, *Crystals* **2018**, *8*, 203.

